Acta Materialia 238 (2022) 118206

Contents lists available at ScienceDirect

Acta Materialia

journal homepage: www.elsevier.com/locate/actamat

Local Phase Transformation Strengthening at Microtwin Boundaries in Nickel-Based Superalloys

A.J. Egan[a,b,*], F. Xue[c], Y. Rao[a], G. Sparks[a,b,d], E. Marquis[c], M. Ghazisaeidi[a,1], S. Tin[e], M.J. Mills[a,b]

[a] Department of Materials Science and Engineering, The Ohio State University, 2136 Fontana Laboratory, 140W 19th Ave, Columbus, OH 43210, USA
[b] Center for Electron Microscopy and Analysis, The Ohio State University, Columbus, OH 43212, USA
[c] Department of Materials Science and Engineering, University of Michigan, 2300 Hayward St, Ann Arbor, MI 48109, USA
[d] Materials and Manufacturing Directorate, Air Force Research Laboratory, Wright-Patterson AFB, OH 45433, USA
[e] Department of Materials Science and Engineering, University of Arizona, 1235 James E. Rogers Way, Tucson, AZ 85719, USA

ARTICLE INFO

Article history:
Received 28 April 2022
Revised 18 July 2022
Accepted 23 July 2022
Available online 25 July 2022

Keywords:
Phase transformation
Creep
Deformation twinning
Electron microscopy
Atom probe tomography (APT)

ABSTRACT

This work investigated two similar polycrystalline alloys, differing by only 1 at% Nb content, which elucidated its effect on local phase transformation strengthening during high temperature creep. Compression creep tests were conducted at 750 °C and 600 MPa to 0.5% strain, resulting in deformation dominated by microtwinning. Higher Nb alloy RRHT5 exhibited superior creep strength to RRHT3 in terms of minimum creep rate. The deformation microstructures were characterized via atomic resolution scanning transmission electron microscopy and energy-dispersive spectroscopy, as well as atom probe tomography, which revealed a novel local phase transformation along microtwin interfaces in RRHT5. Orientation specific cECCI and analysis of superlattice intrinsic and extrinsic stacking faults in this alloy deconvolved strengthening effects of other local phase transformations. Density functional theory calculations complemented the experimental results and suggested this was χ phase formation. Increased creep strength of RRHT5 was attributed to local phase transformation along microtwin interfaces, which inhibited deleterious thickening of microtwins and rapid strain accumulation.

1. Introduction

Nickel-based superalloys are critical structural materials for hot sections of aerospace and land-based gas turbines, where temperatures experienced are in excess of 1600 °C [1–3]. Maximum thrust and fuel efficiency of these turbines strongly depend on the alloy's service temperature, i.e. high temperature strength, which ultimately limits engine efficiency. Increasing the service temperature is therefore a key driving force for research, as well as the desire to reduce harmful CO_2 emissions that exacerbate climate change; an increase of 25 °C can increase efficiency by 1% [4]. Current turbine disks reach average temperatures of ~650 °C, and research thrusts seek to explore properties at temperatures exceeding 700 °C [5,6]. Creep poses a potent restriction on mechanical performance where temperature is the limiting factor, and therefore is a critical area of study [7].

For temperatures in excess of 700 °C, deformation is dominated by thermal activation of planar defects and microtwinning [7–13]. For these mechanisms, diffusion mediated reordering is required, as first pointed out by Kolbe [14] and clarified by Kovarik [13]. It has been observed that segregation of key elements play a major role in these processes, and lead to "local phase transformation" (LPT) at the planar defects [15,16]. As a result of this recent work, it is clear that segregation of Co and Cr plays a prominent role in formation of these defects. Based on density functional theory (DFT) calculations, these two elements serve to lower stacking fault energies (SFE) of complex stacking faults (CSFs) created by shear of a/6 <112> partial dislocations propagating these faults, as well as promoting stability of the remaining superlattice stacking faults (SSFs) via reducing unfavorable Al-Al bonds [9,11,17,18]. Recent research has shown segregation of additional elements Ti, Ta, Hf, and Nb, leading to a potent LPT strengthening effect by formation of η ($D0_{24}$) along superlattice extrinsic stacking faults (SESFs), as first observed by Smith et al. [7,16]. Comparing the creep behavior of ME3 and ME501, these authors found that η LPT formation in the

* Corresponding author.
E-mail address: egan.74@osu.edu (A.J. Egan).
[1] Maryam Ghazisaeidi was an Editor of the journal during the review period of the article. To avoid a conflict of interest, Maryam Ghazisaeidi was blinded to the record and another editor processed this manuscript.

https://doi.org/10.1016/j.actamat.2022.118206
1359-6454/

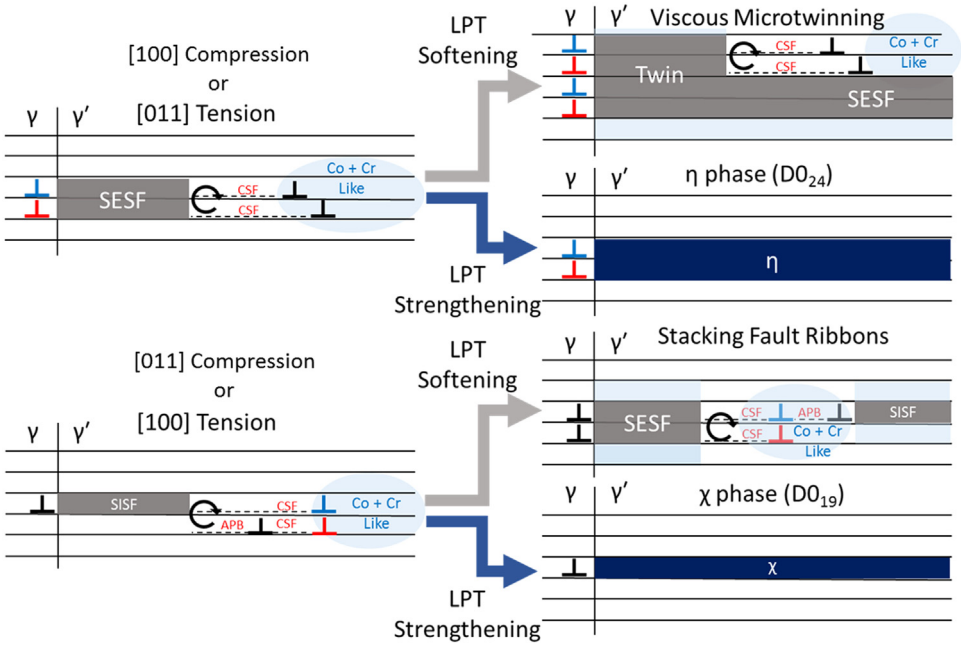

Fig. 1. Summary of orientation dependent fault shearing modes and local phase transformation (LPT) effects.

latter alloy remarkably improved creep resistance; creep strain in ME3 was dominated by microtwinning, whereas ME501 was found to be rich in SESFs decorated with η. These observations suggest that η phase inhibited deleterious thickening of SESFs into microtwins by restriction of additional partial dislocation movement adjacent to the fault. In contrast, microtwin boundaries and SESFs in alloy ME3 featured γ-like LPT with Co and Cr enrichment and produced a softening effect. Additional LPTs have also been discovered along superlattice intrinsic stacking faults (SISFs) in several Ni- and Co-based superalloys by Smith and Titus, respectively [10,12,19–21]. It has been proposed that this DO_{19} χ phase is promoted by Mo and W additions, and also forms bulk precipitates in Co-based superalloys. Creep studies comparing LSHR and ME3 have recently confirmed that χ also serves as an effective strengthener; in grain orientations favoring shear of SISFs and stacking fault ribbons, the CSF/APB segment is inhibited in wake of the leading SISF [12]. Another study involving formation of SISFs from Frank partials in EBROCo-1 has suggested that χ ordering serves to pin the trailing Shockley partial bounding this configuration [22]. The influences of LPT softening and strengthening on deformation characteristics are summarized in Fig. 1, which includes orientation dependencies of their formation [23].

Initial work on RRHT3 and RRHT5 has shown that subtle alloying additions may have profound effect on creep strength [24,25]. These studies compared remarkably strong RRHT5 to RRHT3, which were identical in processing and composition apart from a 1 at% exchange of Nb and Al. RRHT5, with higher Nb content, exhibited slower minimum creep rate than RRHT3. It has been postulated this is related to critical atomic ratios, weighted or otherwise, of Al over LPT formers which lead to increased propensity for LPT strengthening [6]. Lilensten et al. [25] has proposed, based on atom probe tomography (APT) observation, that both η and χ can be activated by increasing Nb content, which was responsible for increased creep strength of high-Nb RRHT5 vs low Nb-RRHT3; however, this was not unambiguously proven as local structure of the faults observed were not assessed. Preliminary work by Egan et al. [24] proposed that this increase in strength was, at least in part, due to a novel LPT affecting microtwin boundaries and inhibiting their thickening in RRHT5. Twins were found to exhibit an ordered HCP motif with segregation of Co and Nb, while being depleted in Ni and Al. However, another key issue with these RRHT studies was that specimens had a 2% strain discrepancy (3% and 1% for RRHT3 and RRHT5, respectively); it is unclear how potent twin-LPT was at preventing additional twin thickening for the same strain level. Thicker twins observed in RRHT3 may have resulted due to increased strain, as well as contribution from multiple slip systems.

The current study seeks to clarify effects of this novel twin-LPT, removing disparities in previous work by comparing compression creep tests at similar strain. Additionally, potential strengthening from η-SESF and χ-SISF LPTs were investigated in each alloy. Post-mortem analysis was conducted using controlled Electron Channeling Contrast Imaging (cECCI) to determine average strain contribution from twins, while high resolution Scanning Transmission Electron Microscopy (HR-STEM) was used to confirm nature of defects formed, probe chemical fluctuation, and determine site occupancies of the LPT. TEM correlated APT was utilized to perform highly accurate chemical analysis at and surrounding defects generated during creep. All experimental analysis was correlated with average grain orientations to isolate each shearing mode illustrated in Fig. 1. Structures investigated were inputs to density functional theory models to support experimental observation.

Table 1
Composition of experimental alloys used in this study.

Alloy	Composition at%								
	Ni	Co	Cr	Al	Ti	Nb	W	Ta	Mo
RRHT5	Bal	18.1	14	8	0	5.5	0.8	1	1.5
RRHT3	Bal	18.3	14	9.8	0	4.6	0.8	1	1.5

2. Materials and methods

2.1. Sample preparation

Alloys used in this study were obtained in as-forged condition from a hot isostatically pressed (HIP) billet. Compositions of RRHT3 and RRHT5 are listed in Table 1.

Both alloys were supersolvus processed at 1170 °C for 1 h and cooled from solution temperature at ~2 °C/s to room temperature, followed by aging at 850 °C for 4 h. As reported elsewhere [24], this resulted in identical microstructure: secondary precipitates with diameters ranging between 250 and 275 nm, as well as some tertiary γ' with 55 nm average diameter that had a minimal impact on an overall volume fraction of ~49%.

Leftover material from fabrication of prior tension specimens was used to make compression creep samples. These were prepared by electric discharge machining (EDM) using a Fanuc ROBOCUT to produce 3 × 3 × 7.4 mm rectangular prisms, which were polished to 1200 grit finish using SiC paper to remove the EDM layer. Testing was performed in a compression creep frame using a vertical clamshell furnace, and conditions from prior 750 °C 600 MPa tension testing were replicated to 0.5% strain following ASTM E139 [26]. A thermocouple adjacent to the specimen was used to monitor temperature throughout the test. Specimens were cooled rapidly by forced air under compression in effort to prevent diffusional or relaxation effects post-test.

2.2. Deformation characterization

Crept specimens were ground through 1200 grit SiC and polished to 0.05 μm colloidal silica finish using an Allied Multiprep such that the scanning electron microscopy (SEM) view was down the compressive axis. Electron backscattered diffraction (EBSD) was conducted in a Thermo Scientific Apreo SEM both to aid in cECCI as well as determine suitable grains for TEM analysis. Platinum was used to mark TEM foils normal to <110> to view planar defects edge-on, and were taken from [001] grains parallel to the compressive axis (//CA) to examine SESF/microtwins. Additional [011]//CA foils were marked to examine SISFs, as well as [111]//CA to examine deformation behavior. Foils were extracted and prepared using an FEI Helios Nanolab Dualbeam 600 focused ion beam (FIB). Nanomilling was conducted using a Fischione Model 1040 Nanomill prior to STEM imaging. A Thermo Scientific Titan or probe-corrected Themis at 200 kV were used for STEM analysis; high resolution EDS was conducted on the Themis using a Super-X EDS system and analyzed with Thermo Scientific VELOX software. Cliff-Lorimer analysis [27] was conducted for EDS quantification using K_α energies for Al, Ni, Co, Cr, Ti, Nb, and Mo, while L_α energies were used for Ta and W. Atomic resolution images were taken utilizing the HAADF detector, providing atomic number (Z) contrast of the atomic columns [28–30]. cECCI was accomplished using MATLAB-based code developed by Gregory Sparks for Apreo systems. This used Euler angles provided from EBSD scans as input to achieve desired diffraction conditions, outputting required tilt and rotation. Manual adjustment was required to achieve optimal contrast. Thermo Scientific MAPS software was utilized to analyze the area of entire [001]//CA grains across the sample cross section. Parameters used for cECCI analysis were 20 keV and 0.1 nA using the concentric backscatter (CBS) detector and 5 mm working distance.

Atom probe tomography (APT) specimens were prepared using a standard lift-out and Ga ion beam thinning process on an FEI Helios 650 Nanolab dual scanning electron microscope (SEM/FIB). APT data acquisition was performed on a Cameca LEAP 5000XR operated in laser mode using a pulse energy of 30–50 pJ, 125–350 kHz pulse rate to keep maximum Dalton range ≤ 120, and 0.5–2.5% detection rate at 50 K. APT data was analyzed using the Atom Probe Suite 6.1 software, and the tip reconstructed was based on fixed shank angle using the evaporation field of Ni at 35 nm/V. The reconstruction parameters (image compression factor and field factor k_f) were adjusted to achieve the consistency of microstructure with SEM/TEM observations. The image compression factor and field factor k_f ranged between 1.2 and 1.7, and between 3.0 and 4.0, respectively.

3. Results

3.1. Compression creep testing

Results of compression creep testing for RRHT3 and RRHT5 may be found in Fig. 2; this includes a plot of strain vs time, as well as strain rate vs time.

Both alloys exhibited similar acceleration in strain rate during the primary creep transient. RRHT5 demonstrated a significantly lower minimum creep rate (MCR) than RRHT3, resulting in 1.69 longer time to reach 0.5% strain. Note that RRHT3 presented a constantly increasing strain rate following the primary transus, whereas RRHT5 had a relatively constant MCR.

3.2. ECCI characterization of deformation

Microtwinning and deformation via planar defects were identified by cECCI in a similar manner to that presented by Zaefferer [31], which details intensity profiles of dislocations, stacking faults, and twins. Examples of cECCI images taken from [001] grains in RRHT3 and RRHT5 may be found in Fig. 3. The [001] oriented grains relative to the compressive axis were determined via EBSD. The different scales of both images in Fig. 3 should be carefully noted with respect to the thickness and density of twins. Supplementary Fig. 1 shows the entire RRHT5 grain.

Grains of [001] orientation observed in RRHT5 were often found to possess only one primary active slip system, while RRHT3 had multiple, interacting slip systems clearly active. This was also true of higher strain tension specimens observed in prior work [24]. Twins were determined by traces that passed through both γ and γ' phases, whereas traces that only exhibited contrast in γ' were counted as SESFs. This method of identification was consistent with previous studies [16]. Both RRHT3 and RRHT5 were dominated by twinning deformation modes, though RRHT5 contained few SESFs. Qualitatively, based on scale of images, twins in RRHT3 were found to be much thicker than those in RRHT5. Density and spacing of twins were inversely related to their thickness.

Analysis similar to that used by Viswanathan et al. [32] and Smith et al. [16] was conducted to quantify the contribution of twinning to the total strain in each alloy, which coupled cECCI results with high resolution STEM observations. This method allowed for improved statistics and representation of several grains across the specimen surface, helping to generalize STEM observations. The strain due to twinning may be given as:

$$\gamma = \frac{N_{twin}\Delta_{ave}}{L},\ \Delta = n|b_p| = na_0\left(\frac{\sqrt{6}}{6}\right)$$

Where $\frac{N_{twin}}{L}$ is the line density of twins along a test line and Δ_{ave} is the average displacement of one twin. Displacement of a single twin is given by the product of thickness, n, in {111} planes and Burgers vector of partial dislocations which form the twin. It is abundantly clear in the literature that microtwins are formed via passage of 1/6<112> partial dislocations [9,23,33–38], whose Burgers vector, b_p, is a function of the lattice parameter a_0.

In this analysis the average thickness of microtwins was determined by randomly selecting 10–15 twins across a large FIB foil (~250 μm^2 viewing area) during HR-STEM examination. This is a 25 μm section taken across an entire [001] grain (e.g. Supplementary Fig. 1), milled 10 µm deep, which gives a representative volume below the ~625 μm^2 viewing area of cECCI. Low magnification STEM images of a FIB foil region may be found in Supplementary Fig. 4, which is representative of the 4 foils observed

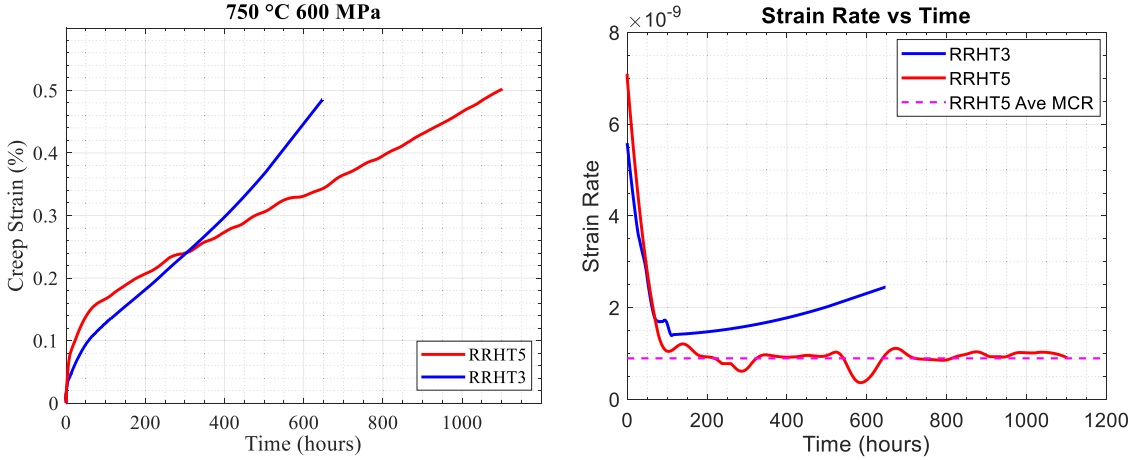

Fig. 2. Compression creep behavior of RRHT3 and RRHT5.

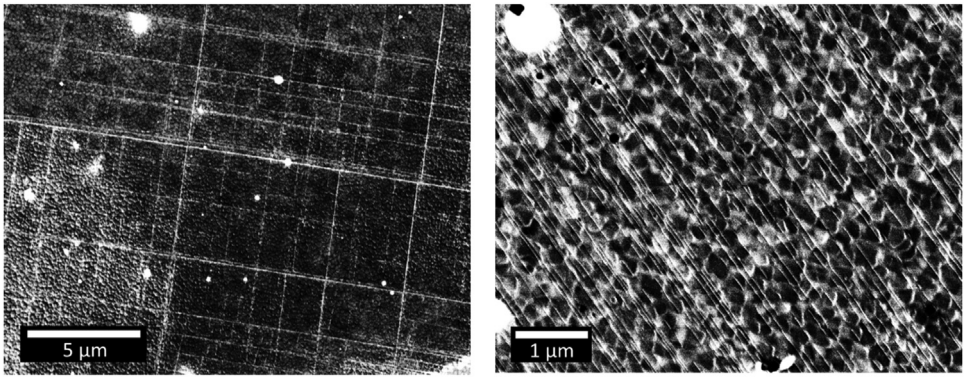

Fig. 3. cECCI micrographs of [001]-oriented RRHT3 (left) and RRHT5 (right).

Table 2
Estimated strain contribution from twining in each alloy based on twin density and thickness in [001] grains.

Twinning Strain Determined by ECCI + STEM					
	Total ECCI Area (μm^2)	Avg Twin Thickness ({111} Planes)	Primary Slip System Strain (%)	Secondary Slip System Strain (%)	Total Strain (%)
RRHT3	1797.5	31.4	0.30%	0.14%	0.44 ± 0.16
RRHT5	437.28	8.2	0.45%	0.07%	0.53 ± 0.20

from [001]//CA grains. Bulk line density was determined in several [001]//CA grains, known to favor SESF/twinning modes of shear [23], across the specimen surfaces using cECCI. Results from combined ECCI and STEM analysis may be found in Table 2, and examples from this may be found in the Supplementary Materials

This confirms that the primary deformation mode in each alloy was indeed twinning, as they accounted for the majority of strain accumulated. SESFs in RRHT5 were minimal in both occurrence and contribution to strain. Twins in RRHT3 were found to be 3.65x as thick on average; representations of typical twins in each alloy are juxtaposed in Fig. 5.

3.3. HR-STEM characterization

Investigation using HAADF STEM was conducted on SESFs and SISFs in each alloy to deconvolve effects of twin LPT from potential η and χ strengthening, respectively. Most observed SESFs in both tension and compression creep of RRHT5 exhibited γ-like LPT, facilitating further thickening into microtwins; though some, similar to Fig. 4c, show η ordering. However, this is not a common observation based on the preponderance of twins examined by ECCI and STEM (Table 2). It can also be noticed that these SESFs possess "patchy" contrast, in other words the η motif is not consistently bright along the fault. This is juxtaposed to SISFs, which are found with prominent χ-LPT as shown in Fig. 4b and 4d.

In the case of RRHT3, the few SESFs found were similar to those in Fig. 4c; the η-like ordering in this case was not as consistent (a denuded "patch" may be seen in the image) as in ME501, NA1 [6,7] or SISFs found in these or other alloys. Generally, SESFs in RRHT3 did not possess much strengthening given their rarity and the rampant twinning observed; it is expected that the few found would be η-decorated. SISFs in RRHT3, however, were prominently decorated and also exhibit local contrast fluctuation from adjacent depletion of heavy elements similar to RRHT5, Fig. 4d, and NA1 [6].

It can be seen from the HAADF STEM images in Fig. 5 that twin boundaries are distinctly different for the two alloys. This imaging mode provides Z-contrast, where heavy elements appear brighter, revealing enrichment to the twin interfaces in both alloys [28–30]; however, RRHT5 is clearly decorated with an ordering pattern following the chevron of the {002} $L1_2$ planes, noticeable from their alternating bright-dark contrast. Additional atomic resolution EDS was conducted of LPT occurring at twin boundaries in RRHT5 and RRHT3, Fig. 6.

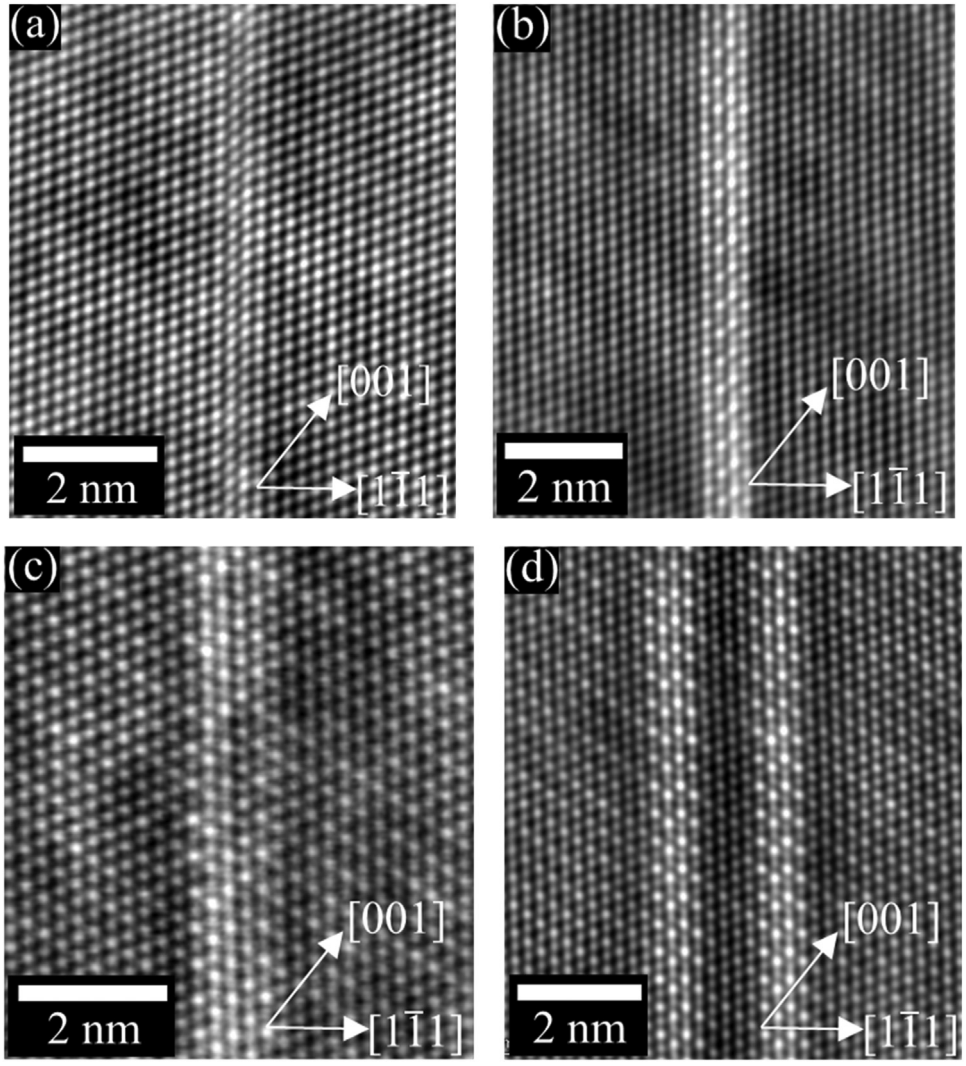

Fig. 4. (a) RRHT5 γ-SESF; (b) RRHT5 χ-SISF; (c) RRHT3 η-SESF; (d) two closely-spaced SISFs in RRHT3 with χ-LPT.

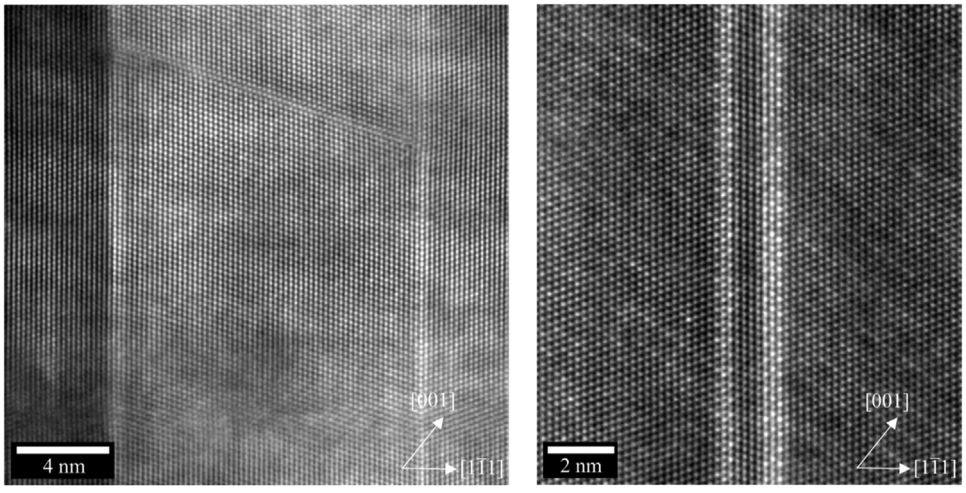

Fig. 5. HAADF STEM images of typical microtwins in RRHT3 (left) and RRHT5 (right).

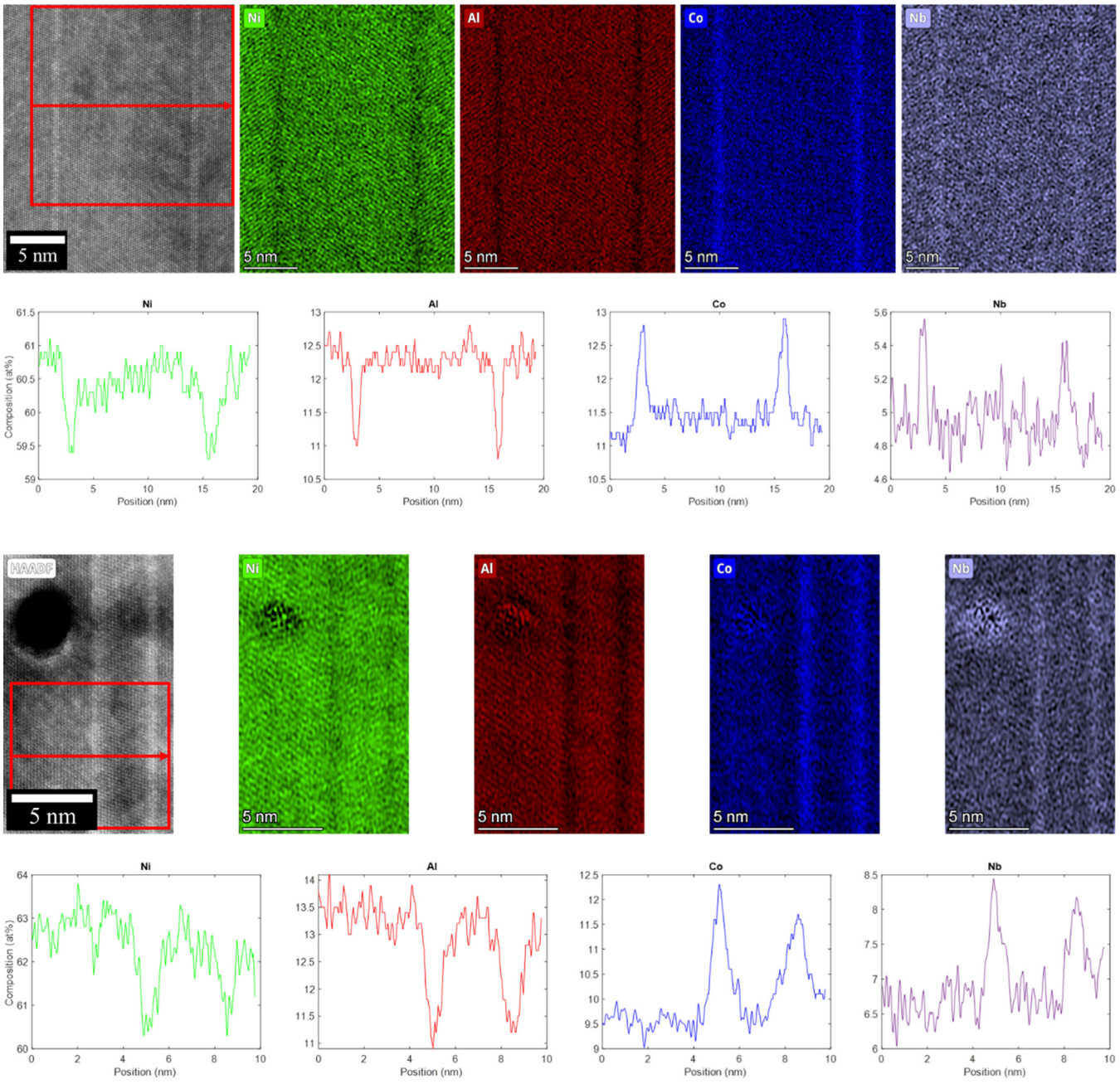

Fig. 6. Low magnification atomic resolution EDS spectra for RRHT3 (top) and RRHT5 (bottom), with corresponding linescans.

Clear depletion of Al and Ni occurs at the twin interface, with corresponding enrichment of Co and Nb. Note that while not shown here, Cr content appears to increase across the entire twin region of RRHT5 by ~0.15 at%. This is atypical, as Cr has previously been shown to segregate to γ-twin interfaces in appreciable ($>$ 1 at%) quantities [7,11,12,35]. The most notable feature is that Nb segregation in RRHT5 (+2%) is greater than 2x that for RRHT3 (+0.6%). Preliminary EDS results conducted by Egan et al. [24] had revealed increased Nb segregation to twin boundaries, with RRHT5 exhibiting a higher concentration than RRHT3.

To elucidate site occupancy and identify the local phase along the twin boundary in RRHT5, spectral maps were averaged over a repeat unit basis defined by the crystal structure of χ/δ for improved resolution of the elements, Fig. 7. This has been proven as an effective method in other works [6,7,39]. From the present $<011>$ viewing projection it was not possible to determine unambiguously between these two structures.

Nb, W/Ta, and Mo were found to prefer Al sites, though the latter is not as obvious. This leaves Co as the primary replacement to the Ni sites, though there appears to be some occupancy for Al sites. Cr is not segregated strongly at the interface, as previously mentioned. While not as clearly segregated as Nb in the line scans, W/Ta and Mo possess increased intensity at the interface, suggesting minute segregation with preference for identical atomic columns fitting the χ/δ motif.

Note that in Figs. 6 and 7, the first atomic resolution chemical maps of a segregated twin boundary with ordered LPT, compositional changes adjacent to the twin were also observed. Similar to first observations along stacking faults in Smith et al. [6], segregation of Co along the twin boundary corresponded to a depletion

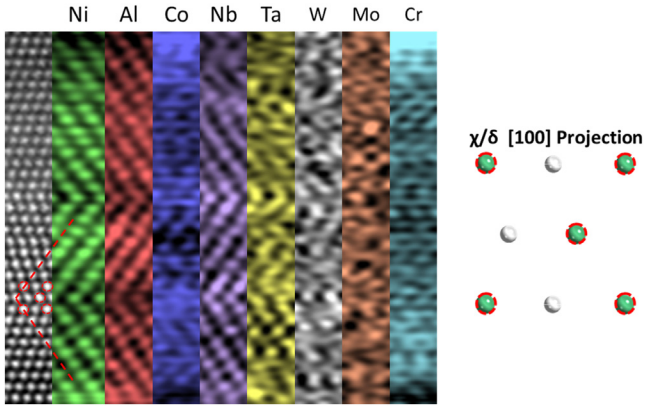

Fig. 7. EDS maps revealing site occupancies along the twin boundary in RRHT5. Dashed circles indicate Nb positions in χ/δ phase, whereas dashed lines indicate <002> chevron of superlattice planes.

in surrounding γ'. In contrast, the opposite was observed for Nb, Al, and Ni, where the depletion at the twin is accompanied by an adjacent enrichment. Note also the twinned region returns to the "baseline" composition for all elements but Co, which is slightly depleted vs the parent γ'. This result confirms recent computational results by Feng et al. [18], which predicted similar chemical fluctuations adjacent to twins. These results all suggest that γ' precipitates present themselves as the primary source for Co segregation to twin boundaries, and as such must also be a source for prior SESFs. This is supported by several previous results showing Cottrell atmospheres leading fault formation [7,11,16,23].

3.4. APT characterization

APT was conducted to compare with and validate STEM/EDS results from RRHT alloys and analyze the potential difference between SESF/SISF LPTs. By preparing samples from both <001>//CA and <011>//CA grains, along with STEM analysis of predominant deformation modes, accurate local composition of SESF and SISFs, respectively, were able to be determined.

One challenge to overcome is not only the large volume of material that must be examined to gather a representative dataset, but also influence of the limited spatial resolution on features of the similar size examined. This happens because of trajectory aberrations and atom surface migration during acquisition, in combination with imperfection in atomic reconstruction, causing anisotropic resolution which is better in axial vs lateral tip directions. In this work, segregation profiles of features in <001>//CA (SESF/microtwinning) grains of RRHT3/5 detected by APT are spread across regions greater than 1 nm, typically 2–3 nm on average, several times larger than the average span of an SESF, 5 {111} planes or ~1 nm found by STEM, Fig. 4. STEM EDS presents a similar spread, though this can be deconvolved to a degree with local structural analysis via HAADF imaging, as well as selection of appropriately thick twins. Comparing the average RRHT5 microtwin thickness of 8.6 {111} planes, 1.72 nm, this is well within the boundaries of a typical segregation peak for a given η-SESF. While this is the typical thickness of RRHT5 microtwins, a true microtwin need only be 4 {111} planes thick at minimum [13]. Note that the region of ordering/segregation on an LPT-twin interface is 3{111} planes, or ~0.6 nm, and is indeed thinner than χ-LPT on SISF, which is 4 planes [10,12]. Therefore, a twin up to ~10 {111} planes, or ~2 nm, could be contained within the broadness of a typical SESF/SISF segregation peak, leading to potential misidentification. The APT technique alone may not be able to distinguish between nature of thin planar defects, as multiple diffraction conditions are not acquired, and these crystallographic structures cannot be accurately reconstructed atom-for-atom [40]. Hence, correlative APT-STEM is necessary when drawing decisive conclusions regarding LPT strengthening, like η, as atomic ordering is a requisite parameter [12,16,21,24].

Fig. 8 shows an SESF and a planar defect in which prominent Co, Nb, Mo, and W segregation was found via APT in microtwin dominant grains ({001}//CA). The SESF segregation matches the trends from STEM-EDS (Figs. 8c and 6), while the other fault exhibits an obviously thicker Cr + Co isosurface (Fig. 8a) and thus stronger segregation (Fig. 8d). Given its nearly doubled absolute concentration and atom excess number of Co and Nb than SESF (Table 4), this fault is most likely a microtwin. Its asymmetric peak of Co and Nb probably results from the overlap of the microtwin's two interfaces, which cannot be deconvolved as that observed by STEM, due to its small thickness (~2.5 nm) and the resolution limit of APT. This is proof from APT that fine microtwins exist and are heavily segregated with Co + Nb, as well as other species. Table 3 presents the typical composition of SESFs in both RRHT3 and RRHT5. It can be seen that SESFs have similar segregation/composition in both alloys, and is confirmed by STEM. Coupled with STEM observation that has shown SISF χ-LPT in both alloys, it can be concluded that neither SESF nor SISF LPT strengthening can explain the enhanced strength exhibited by RRHT5 relative to RRHT3, particularly in {001}//CA grains. In fact, slightly more Nb is found on SESFs in RRHT3 via APT and, therefore, should exhibit greater η strengthening based on empirically calculated phase stabilities [41,42]; this further shows that η strengthening is not the cause of increased strength in RRHT5.

Note also the composition of SISFs in RRHT5 are similar to SESFs but contain more Co. This is almost certainly due to stabilizing χ, $Co_3(Mo,W)$, as it is a stable phase in Co-superalloys where this LPT was originally discovered [19–21]. Nb has recently been suggested in Co-based alloys to stabilize SISF χ-LPT [43–46]. Recent DFT calculations support this suggestion [6]. Given the composition of RRHT5 twin interfaces, this is evidence that a χ phase LPT is present.

Another interesting point is that APT clearly identifies the thick twins in RRHT3, Fig. 9, which also show increased Co and Nb. However, the local increase in Co and Nb is lower than for twins in RRHT5 in terms of atom excess number per unit area (Table 4) and does not routinely cause ordering. The RRHT3 alloy appears to be on the cusp of exhibiting twin-LPT, which is achieved with the minute addition of 1 at% Nb in RRHT5. Intersections of twins also present themselves in RRHT3 APT, with results similar to STEM/ECCI results. This may speak to the ability of twin LPT to interrupt and prevent shearing via planar defects on intersecting slip systems, as evidenced in RRHT5 STEM/ECCI results; the lack of multiple operative systems could also provide explanation for the shorter time to rupture in RRHT5 tension specimens.

3.5. First principles calculation

It is evident from the present STEM and APT observations that a novel LPT has occurred along twin boundaries in RRHT5, similarly to η or χ on SESFs and SISFs, which is juxtaposed to previous twins with deleterious γ formation [7,10,12,16,20]. Similar to η precipitation, the presence of this LPT seems to prevent passage of a/6 <112> partial dislocations along microtwin interfaces that would normally lead to twin thickening and rapid strain accumulation.

From the <110> viewing direction used to view planar defects edge on it is not possible to unambiguously discern the crystal structure of the LPT along the twin interface. Inspection along this direction reveals a D0-type structure at the interface consisting of two interior {111} planes and the adjacent plane outside of the mi-

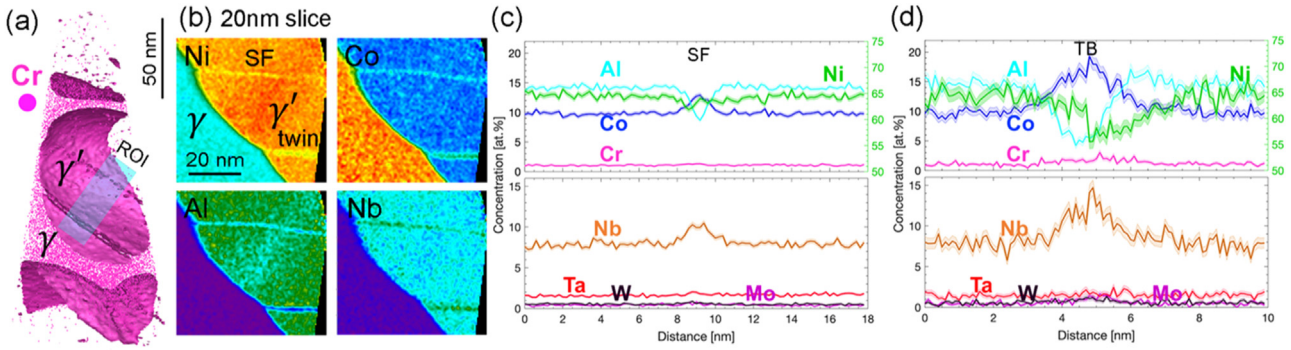

Fig. 8. APT analysis of a tip showing a stacking fault and a microtwin in RRHT5. (a) atomic reconstruction with part of Cr atoms and γ/γ' interface delineated by 14.5 at% (Cr+Co) isosurface; (b) 2D maps of Ni, Co, Al and Nb on a 20 nm slice containing the SF and twin in (a); 1D composition profile across (c) the SF integrated by a $\Phi 32 \times 64 \times 10$ nm^3 cylinder and (d) microtwin by integrating a $\Phi 14 \times 42 \times 10$ nm^3 cylinder.

Table 3
Average atom excess number per unit area (atom/nm^2) of SESF/SISF in RRHT3 and RRHT5.

		Co	Nb	Cr	Mo	W	Ta	Ni	Al
RRHT3	Tension SESF-orientation	3.11 ± 1.21	2.30 ± 0.49	0.35 ± 0.08	0.54 ± 0.11	0.33 ± 0.33	0.20 ± 0.18	−2.85 ± 1.24	−3.98 ± 1.07
RRHT5	Tension SESF-orientation	3.56 ± 0.83	2.66 ± 0.42	0.30 ± 0.26	0.30 ± 0.20	0.18 ± 0.08	0.22 ± 0.07	−3.54 ± 1.10	−3.69± 0.57
	Compression SESF-orientation	2.88 ± 0.72	2.76 ± 0.54	0.10 ± 0.26	0.17 ± 0.16	0.16 ± 0.16	0.17 ± 0.11	−2.75 ± 0.48	−3.50 ± 1.01
	Compression SESF-orientation	3.45 ± 1.00	2.43 ± 0.93	0.38 ± 0.29	0.28 ± 0.07	0.22 ± 0.12	0.05 ± 0.18	−3.33 ± 1.30	−3.48 ± 0.70

Table 4
Atom excess number per unit area ([atom/nm^2]) of SESF and microtwins in RRHT3 and RRHT5.

		Co	Nb	Cr	Mo	W	Ta	Ni	Al
RRHT3	twin	2.77 ± 0.07	2.45 ± 0.07	0.43 ± 0.03	0.43 ± 0.03	0.07 ± 0.01	0.33 ± 0.02	−3.54 ± 0.08	−3.00 ± 0.08
	twin	2.88 ± 0.13	2.64 ± 0.13	0.81 ± 0.07	0.15 ± 0.03	0.03 ± 0.01	0.27 ± 0.04	−3.21 ± 0.14	−4.05 ± 0.16
	twin	1.44 ± 0.05	1.96 ± 0.06	0.32 ± 0.02	0.14 ± 0.02	0.01 ± 0.01	0.34 ± 0.03	−3.72 ± 0.08	−0.57 ± 0.03
	SF	2.88 ± 0.07	2.11 ± 0.06	0.49 ± 0.03	0.34 ± 0.03	0.11 ± 0.01	0.18 ± 0.02	−2.77 ± 0.07	−3.38 ± 0.08
RRHT5	SF	2.71 ± 0.06	2.77 ± 0.06	0.23 ± 0.02	0.24 ± 0.02	0.20 ± 0.02	0.28 ± 0.02	−2.40 ± 0.06	−4.02 ± 0.07
	twin	11.08 ± 0.21	5.94 ± 0.16	1.50 ± 0.08	0.95 ± 0.06	0.57 ± 0.05	0.21 ± 0.03	−10.74 ± 0.21	−9.49 ± 0.20

crotwin. It has been suggested in other systems, albeit with γ'', that twins can be $D0_a$ δ like in nature [53] and this similarity may also be seen in work by Bonnet et al. [55] examining γ'-δ heterointerfaces. While Nb may promote δ, this is not a predominant bulk phase and is not observed along microtwin boundaries as typically would be expected for stable δ alloys [53,54]. As motif cannot be observed through the thickness of the foil, it is also possible that a single unit cell of $D0_{19}$ χ phase could be present, as previously reported on SISFs in this and other alloys [10,12]. Both phases are expected to share the same ordering pattern when viewed in <110> relative to γ', while different viewing in the <112> shearing direction. Unambiguous experimental validation via HR-STEM of the twin-LPT's crystal structure would require this second view and corresponding image simulation, such as μSTEM, which will be addressed in future work.

Instead, we turn to density functional theory to explore the stable phase at the interface. Here, the plane-wave-based density functional theory code VASP [56,57] is used to calculate the energies of the two possible phases at the twin boundary. Pseudopotentials based on the Projector Augmented Wave (PAW) method are used [58]. The exchange correlation is described by Perdew et al. [59] within the generalized gradient approximation scheme. The valence electron configurations are $3d^8 4s^2$, $3s^2 3p^1$ and $5s^1 4d^4$ for Ni, Al, and Nb respectively. A Monkhorst and Pack [60] k-point mesh of $3 \times 3 \times 1$ is used for the Brillouin zone integration. Relaxation of all degrees of freedom is allowed and the convergence criteria are 10^{-5} eV and 5×10^{-3} eV/Å for electronic and ionic steps, respectively. Spin-polarization is enabled in our calculations.

The simulation cell contains 192 atoms, consisting of 12 {111} layers. A twin boundary is introduced at the 7th layer by applying a Burgers vector of $< 11\bar{2} > /3$ on consecutive layers starting from the 8th layer. Then the three layers at the twin boundary are replaced with a 3-layer δ or χ phase. We only have Nb and Ni in these phases for simplification. Both phases are coherent with the γ' matrix. The only difference is the arrangement of Nb atoms, as shown in Fig. 10. Since the calculations involve the same number of atoms, these energies can be compared directly. Our results show that the energy for χ phase is −5.92 eV/atom while for δ phase, it is −5.90 eV/atom. The energy difference of 20 meV/atom suggests that a phase transformation to χ phase is more favorable.

4. Discussion

4.1. Mechanical testing

Results from compression creep tests suggest that the primary creep transient is relatively similar in mechanism and duration, with strain rate accelerating at similar rate. For alloy RRHT5, the transient begins at slightly higher strain rate; therefore, more strain is accumulated at the onset of the minimum creep regime at ∼100 h. This subtle difference here could be due to a slight difference in γ' fraction or size, though this has been found to be minimal [47]. The creep rate during primary creep in superalloys is associated with glide of dislocations in γ channels, which are responsible for configuration of dislocations at γ/γ' interfaces [48–50]; whereas the minimum creep rate regime relates to rate of the prominent γ' shearing mode. The minimum creep rates for these two alloys show marked differences, and therefore rate limiting mechanisms, with RRHT3 exhibiting a constantly accelerating creep rate and RRHT5 remaining roughly constant with time. Based

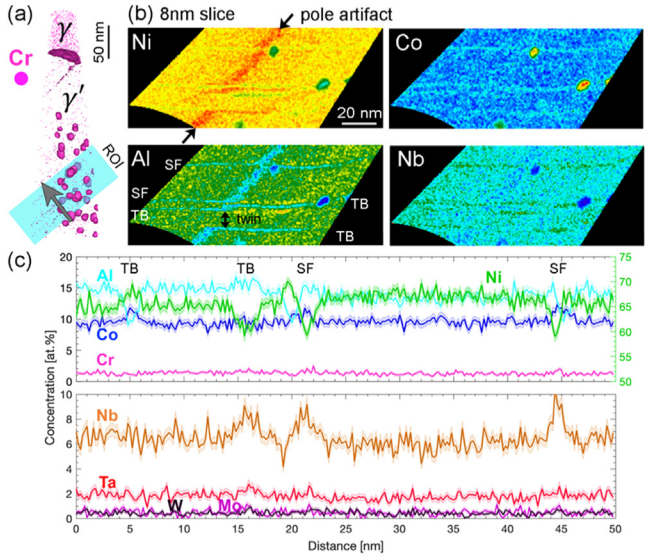

Fig. 9. APT analysis of a RRHT3 tip with SFs and a microtwin. (a) atomic reconstruction with part of Cr atoms and γ/γ' interface delineated by 14.5 at.% (Cr+Co) isosurface; (b) 2D maps of Ni, Co, Al and Nb on a 8 nm slice containing SF and microtwin in (a); (011) pole artifact is marked by black arrows in the 2D map of Ni with a breakdown indicative of microtwin. (c) 1D composition profile across SF and a 15 nm microtwin, as indicated by the gray arrow in (a) and 2D map of Ni in (b), by integrating a $\Phi 20 \times 50$ nm^3 cylinder.

on the experimental results, the explanation for this discrepancy is that RRHT3 exhibits rapid twin thickening, similar to that seen in ME3, whereas RRHT5 benefits from LPT strengthening similar to ME501 [7], preventing this. However, both ECCI and STEM results do not suggest that previously presented LPT strengthening in the literature, i.e. η or χ LPT, can account entirely for the increased creep performance of RRHT5.

4.2. Considerations examining faults/microtwins

It is apparent from the results shown in Fig. 4 that both alloys possess similar levels of η/χ strengthening, though it has been argued in work by Lilensten et al. [25] that η strengthening independently caused increased creep strength in RRHT5. Using context from prior literature comparing γ-LPT and η-LPT on SESFs, an alloy considered "η strengthened" would not be expected to display the high density of twins exhibited by RRHT5. For example, ME501 is the prototypical η-LPT strengthened alloy that is devoid of microtwins, but alloy NA1 also shows this behavior [6,7,16]. STEM results presented here show neither η or χ strengthening alone can explain the difference in high temperature response between RRHT3 and RRHT5.

Several possibilities exist for the discrepancy in RRHT5 behavior relative to this prior work that this paper seeks to clarify: (a) the role of grain specific deformation response, (b) the necessity for HR-STEM characterization, and (c) the influence of LPT-strengthened microtwins. The first point is that orientation of the characterized grains relative to the tensile axis determines operative deformation modes, which has been clearly established in studies on single crystals [23,34,51,52]. These orientation effects have been broadly summarized in Fig. 1, including LPT effects. Without careful consideration of grain orientation when performing ECCI, it is possible to mistake SISFs for SESFs, or vice versa. While it may be theoretically possible to set up multiple diffraction conditions with cECCI to unambiguously determine fault character, confirmation using STEM remains the most direct and accurate method [31]. Utilizing STEM also circumvents near-surface effects that may convolute ECCI results, such as etching that preferentially attacks phases or defects. In this work, grains with [001]//CA were selected for cECCI using EBSD to target only SESF/microtwin dominated grains to definitively determine the effect of potential η-strengthening. Further, these as well as [011]//CA and [111]//CA grains were examined with HR-STEM to definitively determine predominant shear-

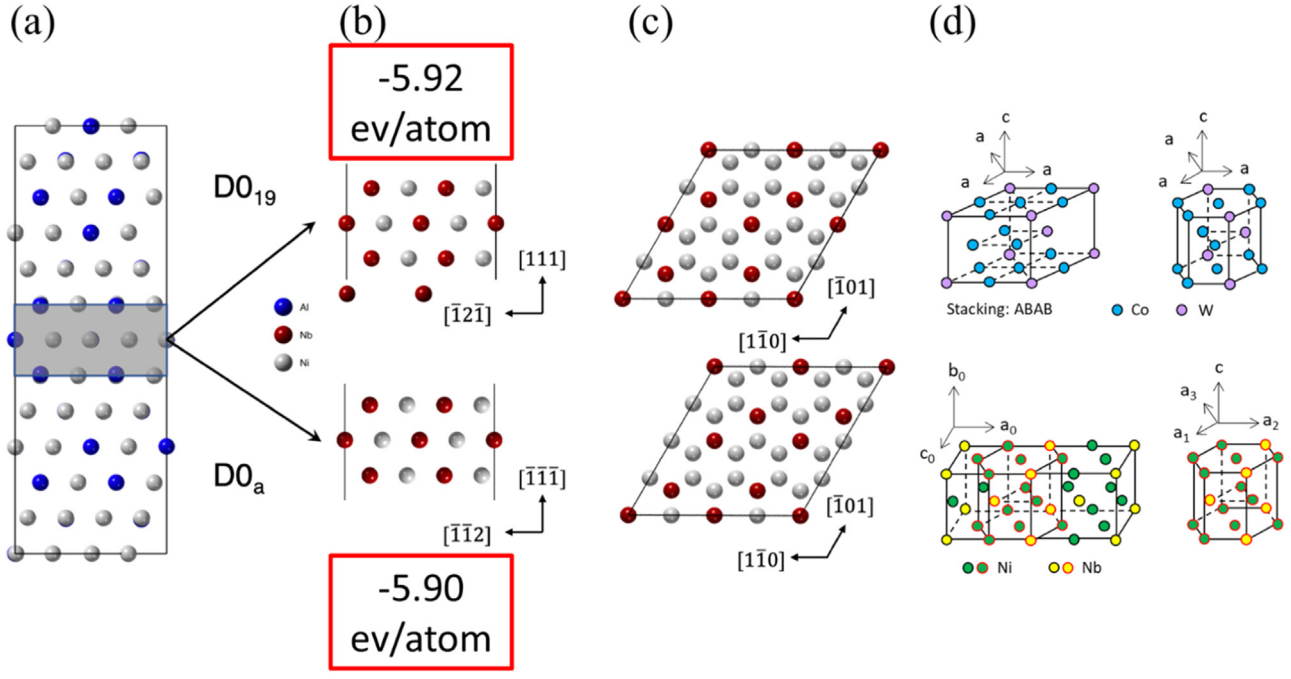

Fig. 10. Simulation cells used in DFT calculation, adapted from [24]. (a) Simulation cell with the twin boundary at the 7th layer. (b) <110> view of the χ phase (top) and the δ phase (bottom). (c) <111> view of the χ phase (top) and the δ phase (bottom). The D0$_{19}$ and D0$_a$ structures differ by relative positions of Nb and Ni atoms not visible in <110> view, as seen in (d) adapted from [61].

Table 5
Phase compositions determined by APT and STEM EDS.

RRHT5, at.%	Ni	Co	Cr	Al	Ta	Nb	Mo	W
nominal	Bal	18.1	14	8	1	5.5	1.5	0.8
APT - γ	31.24 ± 0.01	29.08 ± 0.01	33.25 ± 0.01	1.18 ± 0.01	0.06 ± 0.01	0.86 ± 0.01	2.87 ± 0.01	1.10 ± 0.01
EDS - γ	31.82 ± 6.11	29.54 ± 5.37	30.49 ± 5.55	1.47 ± 0.18	0.13 ± 0.02	0.93 ± 0.17	4.58 ± 0.82	1.03 ± 0.17
APT - γ'	64.83 ± 0.01	9.86 ± 0.01	1.11 ± 0.01	13.93 ± 0.01	1.67 ± 0.01	7.63 ± 0.01	0.42 ± 0.01	0.52 ± 0.01
EDS - γ'	63.76 ± 13.94	10.06 ± 2.11	1.20 ± 0.25	12.72 ± 2.06	1.62 ± 0.31	7.50 ± 1.55	2.46 ± 0.51	0.67 ± 0.13
APT - γ particle	33.53 ± 0.61	29.46 ± 0.58	34.02 ± 0.61	1.26 ± 0.14	0.08 ± 0.04	0.60 ± 0.10	1.24 ± 0.14	–
APT - γ' tertiary	64.76 ± 0.05	10.27 ± 0.03	1.07 ± 0.01	13.48 ± 0.03	1.29 ± 0.01	8.07 ± 0.03	0.36 ± 0.01	0.63 ± 0.01

ing modes in each grain type for these alloys. The [011]//CA and [001]//CA follow trends expected based on single crystal deformation; though other fault types are infrequently observed in HR-STEM.

An important consideration when studying stacking faults and twins is the length-scale of features examined, and the ability of the utilized technique to determine defect character unambiguously. This can be a challenge when using ECCI or methods that only probe composition, such as low-res EDS/EELS, or APT. HAADF-STEM has the advantage of directly identifying features of interest, and may be a reason why coupled/correlated STEM-APT analysis is becoming increasingly popular. Figs. 6 and 7 present a salient example of why this is needed. Depending which element/interface is examined on the EDS spectra/linescan, the observed segregation peak may span between 1.5–2 nm in length; this is roughly the size of the RRHT5 microtwin presented in Fig. 5. Thus, this microtwin could be mistaken for a single fault (one interface) instead of two by utilizing a method with lower resolution like ECCI, or if signal is "smeared", i.e. not discretized, in STEM EDS. Complementary APT performed on compressively crept RRHT5 in this study have also had difficulty teasing out thin twins, and are only found if thicker. Examples are presented in Figs. 8 and 9.

4.3. HR-STEM experiments

Both HAADF STEM and EDS results show intense ordering of heavy elements with clear site preference at the microtwin interfaces. Increased contrast at microtwin boundaries was first suggested by Kovarik et al. [13] in Rene 104, however the periodic intensity variation was not present as in RRHT5 and was similar to RRHT3 or γ-LPT. However, it was noted that Al sites interiorly adjacent to the microtwin interface were out of phase in the "parent" region of the γ', suggesting that Al sites on both sides of the interface were enriched with heavy elements, but not the interface itself. This is juxtaposed to RRHT5, where the interfacial plane as well as adjacent planes showed increased intensity and together exhibited periodic intensity variation akin to an ordered-HCP structure. Ordering of the microtwin interface was only observed in γ' precipitates, comparable to η and χ LPTs. Similar ordering at twin interfaces has been presented by Zhang et al. [53] in a γ-γ'' alloy, who suggested this boundary was a $D0_a$ δ-like region with ABAB stacking. Although this was a γ''-favoring alloy, high Nb content in RRHT5 could favor δ formation locally. This follows logic of Pickering et al. [54] and was used by Smith et al. [16] to justify $D0_{24}$ η precipitation along ABAC-stacked SESFs. However, from <110> views used to observe microtwin interfaces and stacking faults edge on, it is impossible to unambiguously determine the phase via HAADF-STEM; the motif of [100] δ projection is the same as χ observed on SISFs from a <110> γ' zone axis. The only distinct view between the two phases is from a specific <112> view, 90 degrees from the <110> edge on viewing direction, as seen in Fig. 10. This point was used as motivation for density functional theory calculations.

4.4. APT comparison to STEM EDS

Bulk phase compositions for γ and γ' were compared between APT and STEM-EDS analyses to determine if there were any clear variations in compositions between the techniques. This blind comparison provided a clear check to the validity of analysis for both techniques and ensured compositional fluctuations at defects were comparable. Phase compositions are presented in Table 5, including the errors determined for each technique.

4.5. First principles calculations

While not as compositionally complex as the actual alloys, DFT results provide two enlightening points: (1) a Ni_3Nb D0-type phase is energetically favorable and preferred along microtwins vs a Ni_3Al $L1_2$ phase, and (2) this phase is likely χ. Preference for χ (or even δ) here would provide an additional energy barrier against shear of a thickening a/6<112> partials on the adjacent {111} plane just outside of microtwin, due to its ordered-HCP stacking. Additionally, transport of Nb (and Mo, W, Ta which also segregate to microtwins) needing to rearrange after being sheared by a thickening partial may lead to additional viscosity to accumulate strain; a similar phenomenon has recently been suggested as the rate-limiting effect during creep of a Co-Al-W-Ta alloy, due to cross- and in-plane diffusion of W/Ta observed via APT [62]. This was also suggested to slow movement of twin-thickening partials in classic work by Kovarik et al. [13].

A propensity for χ on microtwin boundaries is consistent with previous results that χ has been found to be rich in Nb (Co_3Nb) by several authors studying Co-based superalloys [43–46,63], expanding on the "typical" stoichiometry of Co_3(W, Mo) previously reported for χ LPT. Further support of the ability for Nb addition to stabilize χ is given by the propensity of this LPT to form in SISF-promoting [011]//CA RRHT5 grains and compositional analysis of these SISFs via APT showing enrichment in Co and Nb. Therefore, Nb can be viewed as a potent χ LPT strengthener for both SISFs and microtwin boundaries.

The primary focus of this discussion has been on the verification of a novel strengthening LPT, presumably χ, on microtwin interfaces, and separation of this contribution from other LPTs that could impart strength. Future work will examine this local phase to unambiguously determine its crystal structure via <112> zone axis observations, investigate alternate shearing pathways other than SESFs or SISFs/ribbons that RRHT5 activates resulting from twin-LPT strengthening, and to survey additional compositions and species to promote twin-LPT strengthening.

5. Conclusions

This study compared two alloys, RRHT3 and RRHT5, which were similar except a 1 at% increase of Nb in the latter. The subtle alloying addition in RRHT5 lead to superior creep properties in terms of MCR. Main conclusions via characterization and modeling efforts may be summarized as follows:

- Ordering at twin boundaries has been confirmed via atomic resolution EDS following the motif of D0-type χ or δ. Depletion of Al and Ni was found at the interface, and replaced by segregation of Nb, W/Ta, and Mo on Al sites and Co on Ni sites.
- cECCI+STEM analysis has determined that the primary deformation mode was twinning, as it was estimated to contribute to the majority of accumulated strain based on average microtwin thickness and line density of these defects. RRHT3 was found to exhibit microtwins 3.65x thicker than RRHT5. HAADF-STEM determined that ordering along SESFs/SISFs were similar and contributed limited creep deformation between the two alloys.
- Composition and segregation trends of SESFs/SISFs and microtwins were compared and verified via APT. Microtwins were able to be resolved and match increased segregation found in STEM-EDS. SESFs were found to be more heavily segregated in RRHT3 than RRHT5 based on their background composition, and therefore η strengthening should not be more potent in RRHT5. SISFs were found to be similar, though slightly greater, in segregation of Nb vs SESFs, suggesting Nb activates both η and χ simultaneously.
- DFT calculations of the microtwin interface with and without segregation suggest that χ and δ are both energetically favorable vs γ'. The lower energy of χ implies that this is the stable LPT along microtwin boundaries.
- All the above point to an LPT strengthening along microtwin interfaces. Ordering prevents shear of adjacent a/6<112> partials that would serve to thicken the twin otherwise (if it were γ-LPT). Additionally, lateral transport of heavy elements Nb, Ta/W, and Mo from the microtwin interface that require further reordering may present additional contribution to the rate of strain accumulation.

Future work will seek to unambiguously characterize the LPT structure along microtwin interfaces via <112> zone axis STEM observations, and explore additional deformation pathways that present themselves in response to this novel strengthening mode.

Declaration of Competing Interest

The authors declare that they have no known competing financial interests or personal relationships that could have appeared to influence the work reported in this paper.

Acknowledgements

This work was supported by the National Science Foundation's DMREF program under grant # 1922239. Electron microscopy was performed at the Center for Electron Microscopy and Analysis (CEMAS) at The Ohio State University.

Supplementary materials

Supplementary material associated with this article can be found, in the online version, at doi:10.1016/j.actamat.2022.118206.

References

[1] T.M. Pollock, S. Tin, Nickel-based superalloys for advanced turbine engines: chemistry, microstructure and properties, J. Propuls. Power 22 (2006) 361–374, doi:10.2514/1.18239.
[2] R.C. Reed, The Superalloys: Fundamentals and Applications, Cambridge University Press, 2006, doi:10.1017/CBO9780511541285.
[3] D. Furrer, H. Fecht, Ni-based alloys for turbine discs, J. Met. 51 (1999) 14–17.
[4] R.E.A. Williams, T. Smith, B.D. Esser, N. Antolin, W. Windl, D.W. Mccomb, M.J. Mills, H.L. Fraser, Super-X EDS characterization of chemical segregation within a superlattice extrinsic stacking fault of a Ni-based superalloy, Microsc. Microanal. 21 (2015) 493–494, doi:10.1017/S1431927615003268.
[5] Various, Superalloys 2020, S. Tin, M. Hardy, J. Clews, J. Cormier, Q. Feng, J. Marcin, C. O'Brien, A. Suzuki (Eds.), Springer, 2020.
[6] T.M. Smith, N.A. Zarkevich, A.J. Egan, J. Stuckner, T.P. Gabb, J.W. Lawson, M.J. Mills, Utilizing local phase transformation strengthening for nickel-base superalloys, Commun. Mater. 2 (2021), doi:10.1038/s43246-021-00210-6.
[7] T. Smith, B. Esser, N. Antolin, A. Carlsson, R. Williams, A. Wessman, T. Hanlon, H. Fraser, W. Windl, D. McComb, M. Mills, Phase transformation strengthening of high-temperature superalloys, Nat. Commun. 7 (2016) 1–7, doi:10.1038/ncomms13434.
[8] D. Barba, E. Alabort, S. Pedrazzini, D.M. Collins, A.J. Wilkinson, P.A.J. Bagot, R.C. Reed, On the microtwinning mechanism in a single crystal superalloy, Acta Mater. 135 (2017) 314–329, doi:10.1016/j.actamat.2017.05.072.
[9] T.M. Smith, Y. Rao, Y. Wang, M. Ghazisaeidi, M.J. Mills, Diffusion processes during creep at intermediate temperatures in a Ni- based superalloy, Acta Mater. 141 (2017) 261–272, doi:10.1016/j.actamat.2017.09.027.
[10] T. Smith, B. Esser, B. Good, M. Hooshmand, G. Viswanathan, C. Rae, M. Ghazisaeidi, D. Mccomb, M. Mills, Segregation and phase transformations along superlattice intrinsic stacking faults in Ni-based superalloys, Metall. Mater. Trans. A 49 (2018) 4186–4198, doi:10.1007/s11661-018-4701-5.
[11] D. Barba, T.M. Smith, J. Miao, M.J. Mills, R.C. Reed, Segregation-assisted plasticity in Ni-based superalloys, Metall. Mater. Trans. A 49 (2018) 4173–4185, doi:10.1007/s11661-018-4567-6.
[12] T.M. Smith, B.S. Good, T.P. Gabb, B.D. Esser, A.J. Egan, L.J. Evans, D.W. Mccomb, M.J. Mills, Effect of stacking fault segregation and local phase transformations on creep strength in Ni-base superalloys, Acta Mater. 172 (2019) 55–65, doi:10.1016/j.actamat.2019.04.038.
[13] L. Kovarik, R.R. Unocic, J. Li, P. Sarosi, C. Shen, Y. Wang, M.J. Mills, Microtwinning and other shearing mechanisms at intermediate temperatures in Ni-based superalloys, Prog. Mater. Sci. 54 (2009) 839–873, doi:10.1016/j.pmatsci.2009.03.010.
[14] M. Kolbe, The high temperature decrease of the critical resolved shear stress in nickel-base superalloys, Mater. Sci. Eng. A 321 (2001) 383–387 A319.
[15] G.B. Viswanathan, R. Shi, A. Genc, V.A. Vorontsov, L. Kovarik, C.M.F. Rae, M.J. Mills, Segregation at stacking faults within the γ' phase of two Ni-base superalloys following intermediate temperature creep, Scr. Mater. 94 (2015) 5–8, doi:10.1016/j.scriptamat.2014.06.032.
[16] T. Smith, B. Esser, N. Antolin, G. Viswanathan, T. Hanlon, A. Wessman, D. Mourer, W. Windl, D. McComb, M. Mills, Segregation and eta phase formation along stacking faults during creep at intermediate temperatures in a Ni-based superalloy, Acta Mater. 100 (2015) 19–31, doi:10.1016/j.actamat.2015.08.053.
[17] Y. Rao, T.M. Smith, M.J. Mills, M. Ghazisaeidi, Segregation of alloying elements to planar faults in γ'-Ni3Al, Acta Mater. 148 (2018) 173–184, doi:10.1016/j.actamat.2018.01.055.
[18] L. Feng, Y. Rao, M. Ghazisaeidi, M.J. Mills, Y. Wang, Quantitative prediction of Suzuki segregation at stacking faults of γ' phase in Ni-base superalloys, Acta Mater. 200 (2020) 223–235, doi:10.1016/j.actamat.2020.08.056.
[19] M.S. Titus, Y.M. Eggeler, A. Suzuki, T.M. Pollock, Creep-induced planar defects in L1 2-containing Co-and CoNi-base single-crystal superalloys, Acta Mater 82 (2014) 530–539, doi:10.1016/j.actamat.2014.08.033.
[20] M.S. Titus, R.K. Rhein, P.B. Wells, P.C. Dodge, G.B. Viswanathan, M.J. Mills, A. Van Der Ven, T.M. Pollock, Solute segregation and deviation from bulk thermodynamics at nanoscale crystalline defects, Sci. Adv. 2 (2016) 1–7, doi:10.1126/sciadv.1601796.
[21] M.S. Titus, A. Mottura, G.B. Viswanathan, A. Suzuki, M.J. Mills, T.M. Pollock, High resolution energy dispersive spectroscopy mapping of planar defects in L1 2-containing Co-base superalloys, Acta Mater 89 (2015) 423–437, doi:10.1016/j.actamat.2015.01.050.
[22] M. Lenz, M. Wu, E. Spiecker, Segregation-assisted climb of Frank partial dislocations: an alternative route to superintrinsic stacking faults in L12-hardened superalloys, Acta Mater. 191 (2020) 270–279, doi:10.1016/j.actamat.2020.03.056.
[23] T.M. Smith, R.R. Unocic, H. Deutchman, M.J. Mills, Creep deformation mechanism mapping in nickel base disk superalloys, Mater. High Temp. 33 (2016) 372–383, doi:10.1080/09603409.2016.1180858.
[24] A.J. Egan, Y. Rao, G.B. Viswanathan, T.M. Smith, M. Ghazisaeidi, S. Tin, M.J. Mills, Effect of Nb alloying addition on local phase transformation at microtwin boundaries in nickel-based superalloys, in: The Minerals, Metals & Materials Series, Springer Science and Business Media Deutschland GmbH, 2020, pp. 640–650, doi:10.1007/978-3-030-51834-9_62.
[25] L. Lilensten, S. Antonov, B. Gault, S. Tin, P. Kontis, Enhanced creep performance in a polycrystalline superalloy driven by atomic-scale phase transformation along planar faults, Acta Mater. 202 (2021) 232–242, doi:10.1016/j.actamat.2020.10.062.
[26] , Standard Test Methods for Conducting Creep, Creep-rupture, and stress-rupture tests of metallic materials, ASTM, 2018 https://dx.doi.org/10.1520/E0139-11R18.
[27] H. Hoeft, P. Schwaab, Investigations towards optimizing EDS analysis by the Cliff-Lorimer method in scanning transmission electron microscopy, X-Ray Spectrom. 17 (1988) 201–208, doi:10.1002/xrs.1300170509.
[28] S.J. Pennycook, Z-contrast stem for materials science, Ultramicroscopy 30 (1989) 58–69, doi:10.1016/0304-3991(89)90173-3.
[29] S.J. Pennycook, D.E. Jesson, High-resolution Z-contrast imaging of crystals, Ultramicroscopy 37 (1991) 14–38, doi:10.1016/0304-3991(91)90004-P.
[30] S.J. Pennycook, Z-contrast transmission electron microscopy: direct atomic imaging of materials, Annual Review of Materials Science 22 (1992) 171–195, doi:10.1146/annurev.ms.22.080192.001131.
[31] S. Zaefferer, N.N. Elhami, Theory and application of electron channelling con-

trast imaging under controlled diffraction conditions, Acta Mater. 75 (2014) 20–50, doi:10.1016/j.actamat.2014.04.018.
[32] G.B. Viswanathan, P.M. Sarosi, M.F. Henry, D.D. Whitis, W.W. Milligan, M.J. Mills, Investigation of creep deformation mechanisms at intermediate temperatures in René 88 DT, Acta Mater. 53 (2005) 3041–3057, doi:10.1016/j.actamat.2005.03.017.
[33] R.R. Unocic, N. Zhou, L. Kovarik, C. Shen, Y. Wang, M.J. Mills, Dislocation decorrelation and relationship to deformation microtwins during creep of a gamma' precipitate strengthened Ni-based superalloy, Acta Mater. 59 (2011) 7325–7339, doi:10.1016/j.actamat.2011.07.069.
[34] M. Lenz, Y.M. Eggeler, J. Müller, C.H. Zenk, N. Volz, P. Wollgramm, G. Eggeler, S. Neumeier, M. Göken, E. Spiecker, Tension/Compression asymmetry of a creep deformed single crystal Co-base superalloy, Acta Mater. 166 (2019) 597–610, doi:10.1016/j.actamat.2018.12.053.
[35] L.P. Freund, O.M.D.M. Messï¿½, J.S. Barnard, M. Gï¿½ken, S. Neumeier, C.M.F. Rae, O.M.D.M. Messe, J.S. Barnard, M. Goken, S. Neumeier, C.M.F. Rae, Segregation assisted microtwinning during creep of a polycrystalline L12-hardened Co-base superalloy, Acta Mater. 123 (2017) 295–304, doi:10.1016/j.actamat.2016.10.048.
[36] D. Bürger, A. Dlouhý, K. Yoshimi, G. Eggeler, How Nanoscale Dislocation Reactions Govern Low- Temperature and High-Stress Creep of Ni-Base Single Crystal Superalloys, Crystals 10 (2020) 134, doi:10.3390/cryst10020134.
[37] R.R. Unocic, G.B. Viswanathan, P.M. Sarosi, S. Karthikeyan, J. Li, M.J. Mills, Mechanisms of creep deformation in polycrystalline Ni-base disk superalloys, Mater. Sci. Eng. A. 483 (484) (2008) 25–32, doi:10.1016/j.msea.2006.08.148.
[38] G.B. Viswanathan, S. Karthikeyan, P.M. Sarosi, R.R. Unocic, M.J. Mills, Microtwinning during intermediate temperature creep of polycrystalline Ni-based superalloys: mechanisms and modelling Microtwinning during intermediate temperature creep of polycrystalline Ni-based superalloys: mechanisms and modell, Philos. Mag. 86 (2006) 29–31, doi:10.1080/14786430600767750.
[39] S. Wenner, L. Jones, C.D. Marioara, R. Holmestad, Atomic-resolution chemical mapping of ordered precipitates in Al alloys using energy-dispersive X-ray spectroscopy, Micron 96 (2017) 103–111, doi:10.1016/j.micron.2017.02.007.
[40] Baptiste Gault, Michael P. Moody, Julie M. Cairney, Simon P. Ringer, Atom Probe Microscopy, Springer, New York, NY, 2012.
[41] M. Detrois, S. Antonov, R.C. Helmink, S. Tin, Precipitate phase stability in γ-γ'-δ-η Ni-base superalloys, JOM 66 (2014) 2478–2485, doi:10.1007/s11837-014-1157-y.
[42] S. Antonov, M. Detrois, R.C. Helmink, S. Tin, Precipitate phase stability and compositional dependence on alloying additions in γ-γ'-δ-η Ni-base superalloys, J. Alloys Compd. 626 (2015) 76–86, doi:10.1016/j.jallcom.2014.11.155.
[43] S.K. Makineni, B. Nithin, D. Palanisamy, K. Chattopadhyay, Phase evolution and crystallography of precipitates during decomposition of new "tungsten-free" Co(Ni)–Mo–Al–Nb γ–γ' superalloys at elevated temperatures, J Mater Sci 51 (2016) 7843–7860, doi:10.1007/s10853-016-0026-1.
[44] S.K. Makineni, B. Nithin, K. Chattopadhyay, Synthesis of a new tungsten-free γ-γ' Cobalt-based superalloy by tuning alloying additions, Acta Mater. (2015), doi:10.1016/j.actamat.2014.11.016.
[45] A. Tomaszewska, T. Mikuszewski, G. Moskal, D. Migas, Primary microstructure, microsegregation and precipitates characterization of an as-cast new type g-g 0 Co-Al-Mo-Nb cobalt-based superalloy, Journal of Alloys and Compounds 750 (2018) 741–749, doi:10.1016/j.jallcom.2018.03.397.
[46] F.L.R. Tirado, J.P. Toinin, D.C. Dunand, gamma+gammaprime microstructures in the Co-Ta-V and Co-Nb-V ternary systems, Acta Mater 151 (2018) 137–148, doi:10.1016/j.actamat.2018.03.057.
[47] K. Kakehi, Effect of primary and secondary precipitates on creep strength of Ni-base superalloy single crystals, Mater. Sci. Eng. A 278 (2000) 135–141, doi:10.1016/S0921-5093(99)00579-1.
[48] X. Wu, A. Dlouhy, Y.M. Eggeler, E. Spiecker, A. Kostka, C. Somsen, G. Eggeler, On the nucleation of planar faults during low temperature and high stress creep of single crystal Ni-base superalloys, Acta Mater. 144 (2018) 642–655, doi:10.1016/j.actamat.2017.09.063.
[49] X. Wu, P. Wollgramm, C. Somsen, A. Dlouhy, A. Kostka, G. Eggeler, Double minimum creep of single crystal Ni-base superalloys, Acta Mater. 112 (2016) 242–260, doi:10.1016/j.actamat.2016.04.012.
[50] C.M.F. Rae, R.C. Reed, Primary creep in single crystal superalloys: origins, mechanisms and effects, Acta Mater 55 (3) (2006) 1067–1081, doi:10.1016/j.actamat.2006.09.026.
[51] M. Yamashita, K. Kakehi, Tension/compression asymmetry in yield and creep strengths of Ni-based superalloy with a high amount of tantalum, Scripta Materialia 55 (2) (2006) 139–142, doi:10.1016/j.scriptamat.2006.03.048.
[52] N. Tsuno, S. Shimabayashi, K. Kakehi, C.M.F. Rae, R.C. Reed, Tension/compression asymmetry in yield and creep strengths of Ni-based superalloys, Superalloys 2008 (2008) 433–442, doi:10.7449/2008/Superalloys_2008_433_442.
[53] Z. Zhang, Z. Yang, S. Lu, A. Harte, R. Morana, M. Preuss, Strain localisation and failure at twin-boundary complexions in nickel-based superalloys, Nat. Commun. 11 (2020) 1–11, doi:10.1038/s41467-020-18641-z.
[54] E.J. Pickering, H. Mathur, A. Bhowmik, O.M.D.M. Messé, J.S. Barnard, M.C. Hardy, R. Krakow, K. Loehnert, H.J. Stone, C.M.F. Rae, Grain-boundary precipitation in Allvac 718Plus, Acta Mater. 60 (2012) 2757–2769, doi:10.1016/j.actamat.2012.01.042.
[55] R. Bonnet, M. Loubradou, U. Dahmen, Atomic scale observation of the displacement fields generated by the intrinsic defects of {1 1 1}Ni 3 Al/(0 1 0)Ni 3 Nb close-packed interfaces, Philosophical Magazine A (2000) 2233-2256 , doi: https://doi.org/10.1080/01418610008216471.
[56] G. Kresse, J. Furthmüller, J. Furthmü, Efficient iterative schemes for *ab initio* total-energy calculations using a plane-wave basis set, Phys. Rev. B. 54 (1996) 11169–11186, doi:10.1103/PhysRevB.54.11169.
[57] G. Kresse, D. Joubert, From Ultrasoft Pseudopotentials to the Projector Augmented-Wave Method, American Physical Society, 1999, doi:10.1103/PhysRevB.59.1758.
[58] P.E. Blochl, Projector augmented-wave method, Phys Rev B 50 (1994) 17953–17979, doi:10.1103/PhysRevB.50.17953.
[59] J.P. Perdew, K. Burke, M. Ernzerhof, Generalized gradient approximation made simple, Phys. Rev. Lett. 77 (1996) 3865, doi:10.1103/PhysRevLett.77.3865.
[60] H.J. Monkhorst, J.D. Pack, Special points for Brillonin-zone integrations, Phys. Rev. B. 13 (1976) 5188, doi:10.1103/PhysRevB.13.5188.
[61] L. Feng, A.J. Egan, M.J. Mills, Y. Wang, Dynamic, localized phase transformation at stacking faults during creep deformation and new criterion for superalloy design, MRS Comminications (2022) Submitted for publication.
[62] J. He, C.H. Zenk, X. Zhou, S. Neumeier, D. Raabe, B. Gault, S.K. Makineni, On the atomic solute diffusional mechanisms during compressive creep deformation of a Co-Al-W-Ta single crystal superalloy, Acta Mater. 184 (2020) 86–99, doi:10.1016/j.actamat.2019.11.035.
[63] S.K. Makineni, B. Nithin, K. Chattopadhyay, A new tungsten-free γ-γ' Co-Al-Mo-Nb-based superalloy, Scr. Mater. 98 (2015) 36–39, doi:10.1016/j.scriptamat.2014.11.009.